nature communications

Article

https://doi.org/10.1038/s41467-024-50961-2

Pressure-induced shape and color changes and mechanical-stimulation-driven reverse transition in a one-dimensional hybrid halide

Received: 25 January 2024

Accepted: 23 July 2024

Published online: 06 August 2024

Check for updates

Die Zhang[1,6], Boyang Fu[1,6], Weilong He[1,6], Hengtao Li[2], Fuyang Liu[3], Luhong Wang[4], Haozhe Liu[3], Liujiang Zhou[2,5] ✉ & Weizhao Cai[1,5] ✉

Dynamic crystals with directional deformations in response to external stimuli through molecular reconfiguration, are observed predominantly in certain organic crystals and metal complexes. Low-dimensional hybrid halides, resemble these materials due to the presence of strong hydrogen bonds between bulky organic moieties and inorganic units, whereas their dynamic behavior remains largely unexplored. Here we show that a one-dimensional hybrid halide (MV)$BiBr_5$ (MV = methylviologen) undergoes an isosymmetric phase transition at hydrostatic pressure of 0.20 GPa, accompanied by a remarkable length expansion of 20–30% and red to dark yellow color change. Unexpectedly, the backward transition can be fully reversed by mechanical stimulation rather than decompression. In the high-pressure phase, the coexistence of strong Bi^{3+} lone pair stereochemical activity and large reorientations of the planar MV^{2+} cations, together with the newly formed CH···Br hydrogen interactions, are the structural features that facilitate microscopic changes and stabilize the metastable high-pressure phase at ambient conditions.

Dynamic crystals are a family of crystalline compounds that exhibit a mechanical response when subjected to external stimuli, demonstrating remarkable mechanical motion (for example, bending, jumping, curling, deformation, and rotation) due to the amplification of microscopic perturbation during molecular reconfiguration[1,2]. These intriguing properties allow this type of material to have potential applications in light-weight actuators, sensors, and flexible optoelectronic devices[3,4]. Previous studies have shown that the dynamic behavior typically correlates with rapid martensitic transitions, facilitated by the cooperative rearrangement of the molecular packing[5]. Most dynamic organic crystals and metal complexes undergo such a type of solid single-crystal-to-single-crystal (SC-to-SC) transitions that are reversibly deformed. The original and transformed phases of the martensitic transition exhibit close orientation correlation and similar molecular packing within their crystal structures[6–11]. In addition, another SC-to-SC transition based on the nucleation and growth mechanism has also been reported. In the transformed phase, the structure has been reconstructed and thereby shows a large structural dissimilarity compared to the original phase. The cocrystal 7,7,8,8-tetracyanoquinodimethane-*p*-bis(8-hydroxyquinolinato) copper(II) (CuQ2-TCNQ) serves as a representative example of this type. It shows a 100% increase in single crystal length from form II to form I under mechanical stimulation, demonstrating a slow transition rate attributed to the cooperative movement of the stacked molecular sheets[12].

[1]School of Materials and Energy, University of Electronic Science and Technology of China, Chengdu 611731 Sichuan, China. [2]School of Physics, State Key Laboratory of Electronic Thin Films and Integrated Devices, University of Electronic Science and Technology of China, Chengdu 611731 Sichuan, China. [3]Center for High Pressure Science and Technology Advanced Research, Haidian, Beijing 100094, China. [4]Shanghai Key Laboratory of Material Frontiers Research in Extreme Environments, Shanghai Advanced Research in Physical Sciences, Shanghai 201203, China. [5]Huzhou Key Laboratory of Smart and Clean Energy, Yangtze Delta Region Institute (Huzhou), University of Electronic Science and Technology of China, Huzhou 313001, China. [6]These authors contributed equally: Die Zhang, Boyang Fu, Weilong He. ✉e-mail: ljzhou@uestc.edu.cn; wzhcai@uestc.edu.cn

Most of these examples demonstrate reversible SC-to-SC phase transitions with shape and color modifications induced by light, temperature, pressure or organic vapor[13–16], however, mechanical-stimulation-triggered phase transformations are generally irreversible and the reversed phase changes are rarely reported[12,17,18].

The organic-inorganic hybrid metal halides, which are analogous to molecular crystals due to strong hydrogen bonds between bulky organic parts and inorganic units, typically exhibit reversible SC-to-SC phase transitions and tunable optical properties under variations of temperature and pressure[19–25]. If the metal centers were occupied by stereochemically active ns^2 lone pairs on the M^{2+} or M^{3+} cations, dynamic or static distortion of the local octahedral geometry appeared, which could give rise to distinctive lattice distortions, ferroelectricity, nonlinear optical and emission properties[26–30]. In contrast to dynamic crystals, concurrent dimension and color changes in these materials during the phase transitions are very rare. To date, there is only one example of a two-dimensional (2D) halide $(C_{12}H_{25}NH_3)_2PbI_4$ has been identified, exhibiting reversible size and color changes upon heating[31]. Pressure as an efficient tool, could effectively modulate the structural lattice and hydrogen bonding as well as the electronic structures of hybrid halides, resulting in reversible phase changes in most of cases[32,33]. However, investigations of the mechano-responsive (application of external stress) materials with fascinating dynamic properties in low-dimensional hybrid halides are still rare and unexplored.

Previous studies on the low-dimensional metal halides have shown that pressure can enhance the interactions between the small simple organic cations and the inorganic frameworks, shorten the B-X bond lengths, and consequently tune the optical properties[20]. In contrast to the external pressure, the influence of the steric effect of the small size cations on the structural stability can be negligible. However, the incorporation of large-size organic cations into such a low-dimensional system allows for a dramatic increase in steric hindrance in a confined space, which can easily lead to the distortions of inorganic components (for example, phase transition) when the external temperature and pressure change slightly. In this work, we present a pressure-induced irreversible SC-to-SC transition accompanied by drastic crystal shape and color changes and reversion upon mechanical stimulation in the one-dimensional (1D) hybrid halide $MVBiBr_5$ (MV = methylviologen), with the length of ~10 Å for the planar MV^{2+} cation. In the high-pressure phase, the stereochemical activity of the Bi^{3+} lone pair is activated, half of the planar MV^{2+} cations rotate by *ca.* 90° relative to the *ab* plane and subsequently generate new CH···Br hydrogen bonds, which are probably responsible for the considerable shape change and stabilization of the metastable high-pressure phase under ambient conditions. Remarkably, the transformed phase can revert to the original phase upon mechanical stimulation, as confirmed by single crystal X-ray diffraction, UV-vis absorption spectroscopy, and photoluminescence measurements. The pronounced shape and color alternations of the single crystal during the phase changes can be clearly visualized. Density functional theory (DFT) calculations reveal that the density of states near the Fermi level are similar in both phases, with the C-2p and N-2p states of the organic cation MV^{2+} and the Br-4p state dominated predominantly, which differs largely from that of conventional hybrid halide perovskites.

Results and discussion

The dark red single crystals of $(MV)BiBr_5$ were synthesized by the hydrothermal method at 423 K from the mixture of $BiBr_3$, 4,4′-bipyridine, and concentrated HBr in methanol as described previously[34,35]. At ambient conditions, $(MV)BiBr_5$ crystallizes in the monoclinic $P2_1/c$ space group with lattice parameters $a = 5.8578(2)$ Å, $b = 16.2786(5)$ Å, $c = 10.3856(3)$ Å and $\beta = 100.654(3)°$ ($Z = 2$, referred to as phase β). Upon cooling, phase β undergoes a paraelectric-to-ferroelectric phase transition to the polar phase α (space group $P2_1$) at 243 K, where the Bi^{3+} lone pair becomes stereochemically activated, leading to an increase in the band gap[34]. Both phases have comparable lattice parameters, with only the length of the *c* axis contracts by 0.4% after β-α transition. The crystal structures of the phases α and β consist of the one-dimensional (1D) $BiBr_5$ chains separated by the planar MV^{2+} cations within the *bc* plane (Fig. 1a, b). The CH···Br hydrogen bonding motif remained almost the same in both phases, with the hydrogen atoms from the aromatic ring and the methyl group interacting with the Br atoms of the 1D corner-sharing $BiBr_6$ octahedra propagating along the *a* axis. Hence, based on the crystal habit and the Bravais-Friedel-Donnay-Harker (BFDH) morphology calculations, the crystallographic *a* axis should be parallel to the long direction of the rod-like single crystal (Figs. 2 and 3).

With increasing the pressure, we observed that the β phase stabilizes in a narrow pressure range at room temperature and it transforms to the γ phase as the pressure approaches 0.29 GPa. During the transformation to phase γ, the rod-shaped single crystals of phase β expand largely and visibly along the *a* axis whereas contract across their width, and the color concurrently changes from red to dark yellow (Fig. 3 and Supplementary Fig. 1). Due to the uncertainty of the pressure in the diamond anvil cell (DAC) chamber (0.03–0.05 GPa), the sample can be easily over-compressed at a high compressibility rate (for example, about 4.0–6.0 GPa/h) and the β phase transforms directly into the γ phase in most cases (Supplementary Movies 1 and 2). However, the limited space in the DAC chamber (~0.03 cm^2) makes measuring the actuation force during the phase transformation under pressure challenging. Nevertheless, we clearly observed that the force generated during the phase transition could push a small metal piece to the chamber wall (Supplementary Movie 3). It is well-known that the compression rate plays a crucial role in the kinetic effects of pressure-induced phase transformations of the solids in the *P-T* phase diagrams[36,37]. Therefore, we attempted to load several single crystals of different dimensions into DAC chambers and compressed them at very slow rate (for example, about 0.2 GPa/h). Consequently, we observed the coexistence of phases β and γ at ~0.20 GPa with a noticeable color difference, and the phase transition process lasted for over 12 h (Fig. 3b, Supplementary Fig. 1d and Supplementary Movie 4). This observation together with the large alternations in the packing arrangements of the MV^{2+} cations, reveals that the β-γ phase transition is not of the martensitic type but can be classified as the nucleation and growth mechanism[38,39]. Moreover, we found that the length of all ten crystals was significantly elongated in the range of 20–30% along the *a* axis after the completion of the β-γ transition (Supplementary Fig. 1 and Supplementary Table 1). This magnitude is almost four times larger than that of the ~6% length elongation in the 2D halide $(C_{12}H_{25}NH_3)_2PbI_4$ during the thermally induced phase transition[31]. As can be inferred from previous high pressure studies, most crystalline materials tend to shrink in length during phase transitions (positive compressibility). However, there are few additional examples where this dynamic behavior has been noted[15,40,41], making $(MV)BiBr_5$ a very rare example that shows a large expansion of its length during a phase transition.

From the high-pressure single crystal X-ray diffraction (SXRD) measurements at room temperature, the γ phase is determined to have the same space group $P2_1/c$ as the β phase, but with expansions of all the lattice parameters *a*, *b* and *c* (at 0.29 GPa, $Z = 4$, $a = 6.0975(6)$ Å, $b = 17.292(2)$ Å, $c = 17.8464(18)$ Å and $\beta = 97.748(7)°$), resulting in a significantly different crystal structure compared to the β phase (Fig. 1). The centrosymmetric nature of phase γ was also verified by the second harmonic generation (SHG) measurements, which showed no SHG signal over the 300–1200 nm range (Supplementary Fig. 2). Moreover, synchrotron powder X-ray diffraction data were also collected up to 10.54 GPa at room temperature to investigate the phase stability of the sample (Supplementary Figs. 3 and 4). A pronounced volume collapse of ~2.8% for SXRD (~3.3% for PXRD) appears during the

https://doi.org/10.1038/s41467-024-50961-2

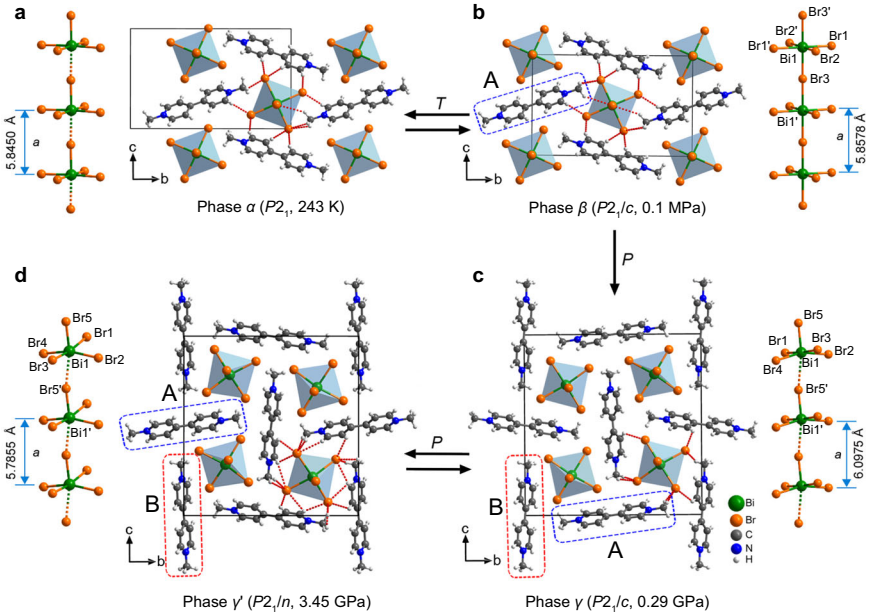

Fig. 1 | Crystal structures of (MV)$BiBr_5$ viewed along the [100] direction. a Phase α at 0.1 MPa/243 K[34]. **b** Phase β at 0.1 MPa/296 K. **c** Phase γ at 0.29 GPa/296 K. **d** Phase γ' at 3.45 GPa/296 K. The 1D $BiBr_5$ chains of four phases are displayed for comparison. The CH···Br hydrogen bonds are shown as red dashed lines in all phases.

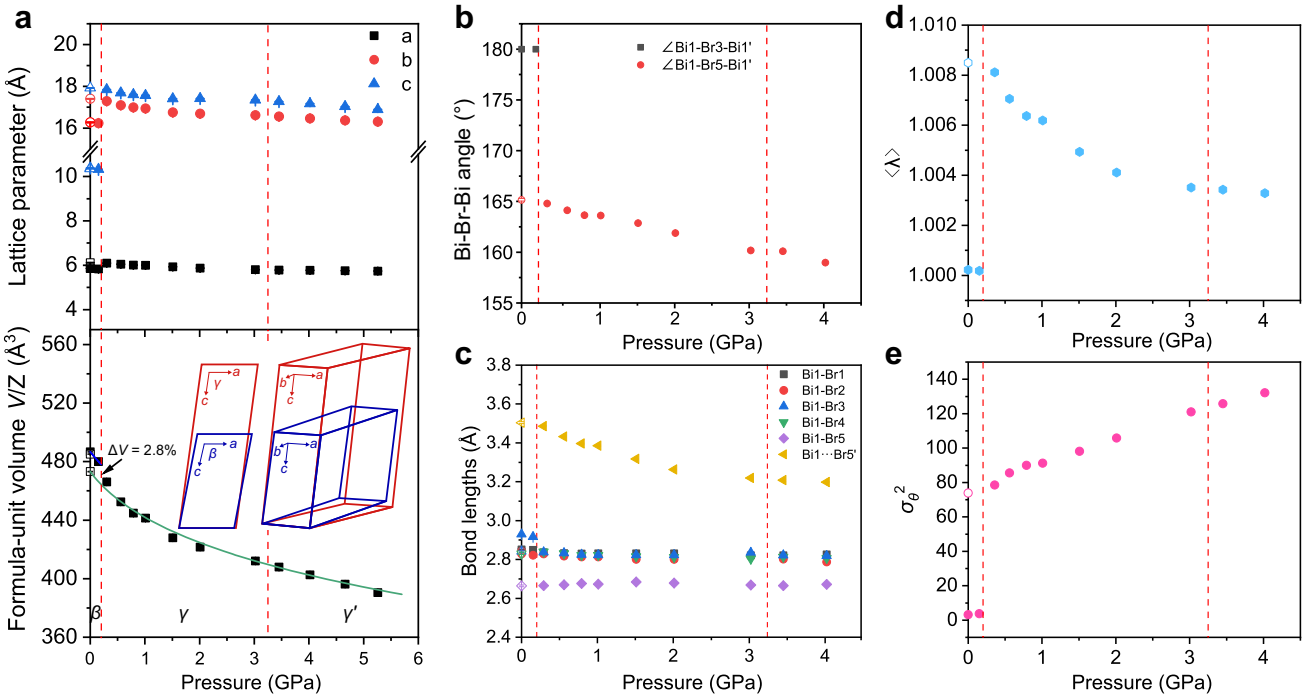

Fig. 2 | Unit-cell dimensions and structural parameters of (MV)$BiBr_5$ under pressure. a Lattice parameters as a function of pressure. The third-order Birch-Murnaghan equations of states (EOS) fit to the formula-unit volume (V/Z) data of phase γ and γ'. The inset shows the unit-cells before and after phase transition viewed along different directions. **b** The pressure dependence of the Bi-Br-Bi′ bending angle between the $BiBr_6$ octahedra in three phases. **c** Changes of Bi-Br bond lengths as a function of pressure. **d**, **e** Evolution of average quadratic elongation ($\langle\lambda\rangle$), and average bond angle variance (σ_θ^2) under compression. Note that the error bars were obtained from the SXRD experiments and the phase transitions at 0.20 and 3.25 GPa are indicated as red dashed lines.

https://doi.org/10.1038/s41467-024-50961-2

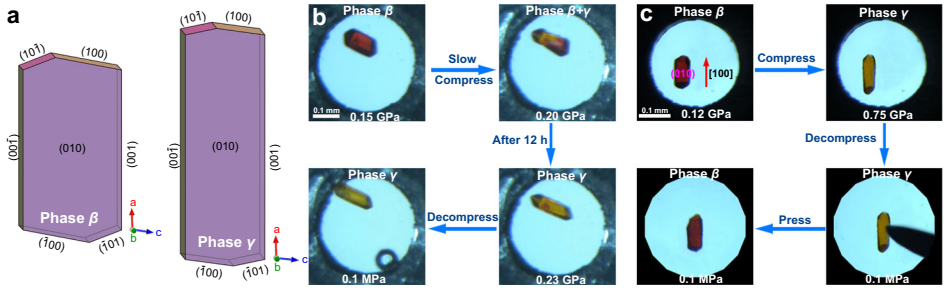

Fig. 3 | Changes in dimensions and color of (MV)$BiBr_5$ single crystals under external stress. a The predicted single crystal morphologies of phases β and γ based on BFDH model. **b** A single crystal was slowly compressed from 0.15 to 0.20 GPa (~0.2 GPa/h) and the coexistence of phase β to γ was observed. The phase β was completely transformed to γ over ~12 h and this phase was maintained after the pressure release to ambient pressure (see air bubbles). **c** A single crystal was compressed from 0.12 GPa (β phase) to 0.75 GPa (γ phase) in the DAC chamber and depressurized to 0.1 MPa. The γ phase reverts back to the β phase after mechanical stimulation (poking with a needle). The scale bars (white bars) are displayed in both **b** and **c** panels.

β-γ transition, which is typical characteristic of a first-order phase transition. At ~3.25 GPa, phase γ transforms to γ' without discontinuous changes in lattice parameters a, b and c, but the β angle starts to decrease under compression in phase γ' region (Fig. 2a and Supplementary Fig. 5). We attempted to use the γ phase structure model to refine the diffraction data of the γ' phase but were unsuccessful. Finally, the γ' phase is determined to be the $P2_1/n$ space group, and the γ-γ' transition can be considered as a second-order phase transition with subtle changes in the lattice parameters (Fig. 2). The γ' phase was observed to survive at least up to 10.54 GPa, as evidenced by the high-pressure PXRD measurements (Supplementary Fig. 3). In phase γ, the lattice parameters exhibit anisotropic compression, with the a-axis identified as the softest axis, which is primarily attributed to the presence of the highly compressible 1D $BiBr_5$ chains (Supplementary Fig. 6). For the SXRD measurements, the magnitude of the strain tensor β_1 is 22.6(12) TPa^{-1}, which is inclined by 17.8° to the a axis, and it is 1.3 times of that along the b axis (where β_b = 17.4(13) TPa^{-1}). The weakest compressibility is approximately along the c axis (inclined by 20.3°), with compressibility coefficient β_3 of 10.3(16) TPa^{-1}, which is half of that of β_1. Fitting the unit-cell volume of phase γ to the third Birch-Murnaghan equation of state yields a zero-pressure bulk modulus B_0 of 8.5(7) GPa and pressure derivative B' of 16(2). These magnitudes are comparable to those obtained from PXRD data (B_0 = 13(1) GPa and B' = 10(2)), as well as those of typical organic solids, but smaller than those of the low-dimensional halides[19,42,43].

In order to gain insight into the elastic properties of the γ phase, we employed the DFT method to calculate the full elastic constants. For the $P2_1/c$ monoclinic system, there are 13 independent elastic constants and the corresponding linear compressibility (β), bulk modulus (B), Young's modulus (E), shear modulus (G) and Poisson's ratio (ν) are presented in Supplementary Tables 2 and 3, respectively. The maximum and minimum values of the elastic constants were obtained to verify the directional contribution using the ELATE software[44]. Due to the distinctive structural characteristics, the sample exhibits pronounced anisotropy in its elastic properties. As shown in Supplementary Fig. 8a, the calculated minimum and maximum magnitudes of linear compressibility are 18.04 TPa^{-1} and 33.24 TPa^{-1}, respectively, and their directions are approximately along the $[10\bar{2}]$ (inclined by 26.5° to the c axis) and [201] (inclined by 26.5° to the a axis). These values are in good agreement with the experimental observations (Supplementary Fig. 6). Moreover, the calculated bulk modulus B of the γ phase was found to be 12.80 GPa, which is reasonably close to the experimental values of 8.5(7) GPa (SXRD data) and 13(1) GPa (PXRD data). In addition, significant anisotropy is also found in E, G and ν. For more detailed discussions, please refer to Supplemental Note 1.

Unlike conventional hybrid halides, which commonly exhibit elastic behavior under external temperature and pressure (that is, reversible SC-to-SC phase transition with imperceptible shape changes)[19,45–47], the (MV)$BiBr_5$ crystal shows a very intriguing dynamic behavior. Unexpectedly, the transformed single crystal could not return to its original shape and color after the pressure was released to ambient pressure, revealing the irreversible character of the sample (Fig. 3, Supplementary Fig. 3, and Supplementary Video 2). Regardless of whether the pressure reached was in the γ or γ' (>3.25 GPa) phase region, all the recovered single crystals were conclusively identified as the γ phase by both SXRD and PXRD measurements (Supplementary Fig. 3 and Supplementary Table 4). Interestingly, when the (010) plane of the γ phase single crystal was pricked with a needle at room temperature, the single crystal alters its shape and color, and immediately transformed back to the β phase and its original shape, indicating that the γ phase is the metastable form at ambient conditions (Fig. 3c and Supplementary Table 5). We calculated the energy difference between phase β and phase γ to be 2.60 kJ/mol at ambient pressure, a value comparable to that observed in the most molecular crystals, for example, glycine[48,49]. The calculations suggest that the γ phase is a metastable phase at ambient conditions, whereas the β phase is the thermodynamically favored form. In order to gain insight into the irreversible γ-to-β phase transition mechanism, we propose a potential transition pathway with seven intermediate states generated by using interpolation method between γ and β phases. The proposed path gives rise to an activation energy barrier of ~290 meV/atom, which is most likely attributed to the large size of MV^{2+} cations and strong CH···Br hydrogen interactions within the lattice (for specific discussions, please refer to Supplementary Fig. 7 and Supplementary Note 2). When the local stress on the (010) face of phase γ is applied, β phase nuclei are initially produced and they diffuse across the entire crystal body, subsequently rearranging to the β phase through the reorientations of large MV^{2+} cations, which initiates the irreversible γ-β phase transition. Consequently, the distinct changes in color and dimensions are observed during the phase transformation (Fig. 3c). Previous studies on mechanical-stimulation-triggered SC-to-SC phase transitions are mainly on molecular crystals and metal complexes, with limited explorations in the hybrid halides. Typically, these phase changes result in the concomitant considerable shape and emission color modifications, as exemplified by phenomena like the "molecular domino" observed in arylgold(I) isocyanide complexes[12,17,50,51]. Therefore, (MV)$BiBr_5$ represents the extremely rare example of a pressure-induced irreversible SC-to-SC transformation and mechanical-stimulation-driven backward transition in 1D hybrid halides.

To understand the origin of the remarkable alternations in crystal dimensions during the β to γ transition, we determined the crystal structures before and after the transformation using high-pressure SXRD. In phase β, there is one type of MV^{2+} cation in the asymmetric unit (group A), whereas in phase γ there are two (group A and B). The

packing orientations of the planar MV^{2+} cations can be described by the dihedral angles φ_1 and φ_2 relative to the *ab* plane, respectively. The dihedral angle φ_1 in phase β is 39.6(2)° and it decreases to 37.4(6)° as the pressure increases from 0.1 MPa to 0.15 GPa (Supplementary Fig. 9). After the transition from phase β to γ, pronounced structural rearrangements are observed: MV group A undergoes a slight clockwise rotation, resulting in a smaller dihedral angle relative to the *ab* plane and still maintaining the "lying down" position, for example, φ_1 equals 28.9(6)° at 0.29 GPa. These small rotations of the MV group A can be explained by the ~7.1% expansion of the length of the *b* axis. However, an intriguing nearly 90° rotation of the MV group B is observed, and it transforms into a "standing up" position with a dihedral angle φ_2 of 89.5(4)°, contributing to a substantial ~72% expansion of the length of the *c* axis (Fig. 1d). The dihedral angles φ_1 and φ_2 decrease slightly under compression in the γ phase region and they maintain a similar trend in the γ' phase. In β phase, the adjacent Bi1···Bi1′ distance within the nearly regular corner-sharing $BiBr_6$ octahedra equals the lattice parameter *a* and it considerably elongates in phase γ due to activation of Bi^{3+} $6s^2$ lone pair stereochemical activity. The extent of the $BiBr_6$ octahedral distortion can be qualified by the quadratic elongation ($\langle\lambda\rangle$) and bond angle variance (σ_θ^2), which are defined as follows:

$$\langle\lambda\rangle = \sum_{i=1}^{6}(l_i/l_0)^2/6 \quad (1)$$

$$\sigma_\theta^2 = \sum_{i=1}^{12}(\theta_i - 90^\circ)^2/11 \quad (2)$$

where l_i is the Bi-Br bond length, l_0 is the average Bi-Br bond length, and θ_i is the Br-Bi-Br bond angle of neighboring bromides[52]. As shown in Fig. 2d, e, the octahedral distortion parameters $\langle\lambda\rangle$ and σ_θ^2 for the nearly regular $BiBr_6$ octahedra in phase β are (1.0002, 3.24) at ambient pressure. These values subsequently change to (1.0001, 3.78) as the pressure increases to 0.15 GPa, indicating enhanced Bi-Br covalent contacts. After the lone pair expression emerges in the polar phase α (0.1 MPa/243 K), the magnitudes of $\langle\lambda\rangle$ and σ_θ^2 are (1.0021, 6.18), indicating that the $BiBr_6$ octahedra become more distorted compared to phase β. In phase γ, the packing rearrangements of the MV cations result in the Bi-Br_{axial} bonds having one short (Bi1-Br5) and one elongated (Bi1•••Br5′) along the *a* axis. At 0.29 GPa, the Bi1•••Br5′ bond length is 3.486(3) Å, exceeding the sum of $r_{Bi^{3+}} + r_{Br^-}$ = 2.99 Å, which indicates the weak bonding. Upon compression, the Bi1•••Br5′ distance gradually reduces from 3.486(3) Å (at 0.29 GPa) to 3.219(5) Å (at 3.02 GPa), whereas the short Bi1-Br5 distance remains relatively unchanged (2.665(3) *vs.* 2.669(5) Å). The other four Bi-$Br_{equatorial}$ bond distances are comparable to those found in phase β and they are difficult to compress under pressure (Fig. 2c). Substantial changes in the $\langle\lambda\rangle$ and σ_θ^2 values are observed during the β-γ transition: they suddenly shift to (1.0081, 78.65) at 0.29 GPa, and then change monotonically with increasing the pressure to (1.0035, 121.12) at 3.02 GPa, and this trend is preserved even in the phase γ' region. The decrease in the $\langle\lambda\rangle$ is attributed to the reduction of Bi1-Br5′ distance under pressure as mentioned above, whereas the increase of σ_θ^2 value is caused by the large distortions of the $BiBr_6$ octahedra (Fig. 2). In contrast to phase β, the phase γ exhibits large magnitudes of octahedral distortion parameters, revealing that the $BiBr_6$ octahedra are more distorted and stronger lone pair stereochemical activity of the Bi^{3+} cations. It is clear to see that there are one short, one long and four intermediate Bi-Br bonds within the $BiBr_6$ octahedra, and the lone pair orbital should extend along the direction of Bi1•••Br5′ bond as notified from the Brown's model[53]. Moreover, the Bi-Br-Bi′ angle between the corner-sharing $BiBr_6$ octahedra along the *a* axis also undergoes abrupt changes during phase transition. For example, the Bi-Br-Bi′ bending angle is equal to 180° in phase β, and it suddenly drops to 164.79(8)° at 0.29 GPa after the phase β-γ transition. Subsequently, it reduces monotonically throughout the entire phase γ region (by ~4.6° up to 3.02 GPa, see Fig. 2b). These observations emphasize the close correlations between the single crystal dimensions, MV^{2+} cations packing arrangements, Bi^{3+} $6s^2$ lone pair expression and the $BiBr_6$ octahedral distortions.

The considerable reorientations of the MV^{2+} cations in phase γ lead to the formation of new hydrogen bonding patterns: the 1D $BiBr_6$ octahedra interacting with the CH donors from the aromatic ring and the methyl group of the MV^{2+} cations (group A and B, see Fig. 1c). From the released phase γ at ambient pressure, the CH•••Br distance ranges from 2.778 to 3.027 Å, which is comparable to that of phase β (2.792-3.017 Å). These observations imply that the strong CH•••Br hydrogen bonds could stabilize the crystal structure of phase γ at ambient pressure, thereby locking the metastable high-pressure structure and resulting in the irreversibility of the transition upon decompression[54]. However, when external stress is applied to the (010) face of the metastable phase γ, that is, the perpendicular direction where the CH•••Br hydrogen bonds dominate the MV^{2+} packing (1D $BiBr_5$ chains), it leads to hydrogen bond breaking and results in the alternations of the packing arrangements of the MV^{2+} cations (especially group B), thus driving the transformation of the metastable phase γ into the thermodynamically more stable phase β (Supplementary Fig. 10). Due to the more compacted structures in phase γ', more CH•••Br hydrogen bonds were formed, generating different hydrogen bonding patterns compared to phase γ (Fig. 1). The CH•••Br interactions in all three phases are gradually enhanced with increasing the pressure, and their evolutions under compression can also be clearly illustrated from the differences of Hirshfeld surfaces and two-dimensional (2D) fingerprint plots (Supplementary Figs. 11 and 12). In phase β, large red areas appear around the CH group within the aromatic ring, indicative of strong H•••Br bonding (Supplementary Fig. 12). In phase γ, there are two different MV groups within the structure and they show different Hirshfeld surfaces compared to phase β due to the newly formed CH•••Br hydrogen bonds (for example, C12H12C•••Br4, C10H10•••Br1). With increasing pressure, the distances of the H•••Br contacts shortened, characterized by the larger red areas on the Hirshfeld surface at 3.02 GPa. The relative contributions of the H•••Br contacts in MV group A and B are 39.7% and 41.3%, respectively, and they decrease to 36.6% and 37.1% as the pressure increases from 0.29 to 3.02 GPa within the phase γ region (Supplementary Fig. 13). The 2D fingerprint plots of phases β and γ contain one sharp spike corresponding to the strong CH•••Br hydrogen bond interactions and they are strongly enhanced under compression (see the shorter d_i and d_e distances in Supplementary Fig. 12).

During the β-γ transition of (MV)$BiBr_5$, the strong Bi^{3+} lone pair expression and rearrangements of MV^{2+} cations caused the crystal color to change abruptly from red to dark yellow, indicative of the electronic band gap alternations. The correlation between the lone pair stereochemical activity of Bi(III), Sn(II) and Pb(II) and the band gap has been observed in a several organic-inorganic hybrid halides[30,34,55,56]. To explore the variation of the band gap under pressure, in situ UV-vis absorption measurements were performed up to 9.78 GPa. At ambient pressure, the band gap of the β phase is 2.12 eV and its absorption edge exhibits a red shift under compression due to the shortening of the Bi-Br bond lengths (Fig. 2c). At transition pressure of 0.20 GPa, a sudden blueshift was observed with the energy band gap increases about 0.26 eV (Fig. 4a). With increasing pressure to 9.78 GPa within the γ' phase region, the single crystal color gradually darkens and changes to dark brown. Simultaneously, the band gap monotonically decreases to 2.17 eV, which is still larger than that of the β phase at ambient pressure (Fig. 4a, c). It is well known that the reduction of the B-X bond lengths generally reduces the band gap, whereas the distortion and tilting of the BX_6 octahedra play an opposite role in metal halides[57,58], such a rule also applies in the (MV)$BiBr_5$. Interestingly, the γ phase could be completely recovered upon pressure release to ambient pressure, with

https://doi.org/10.1038/s41467-024-50961-2

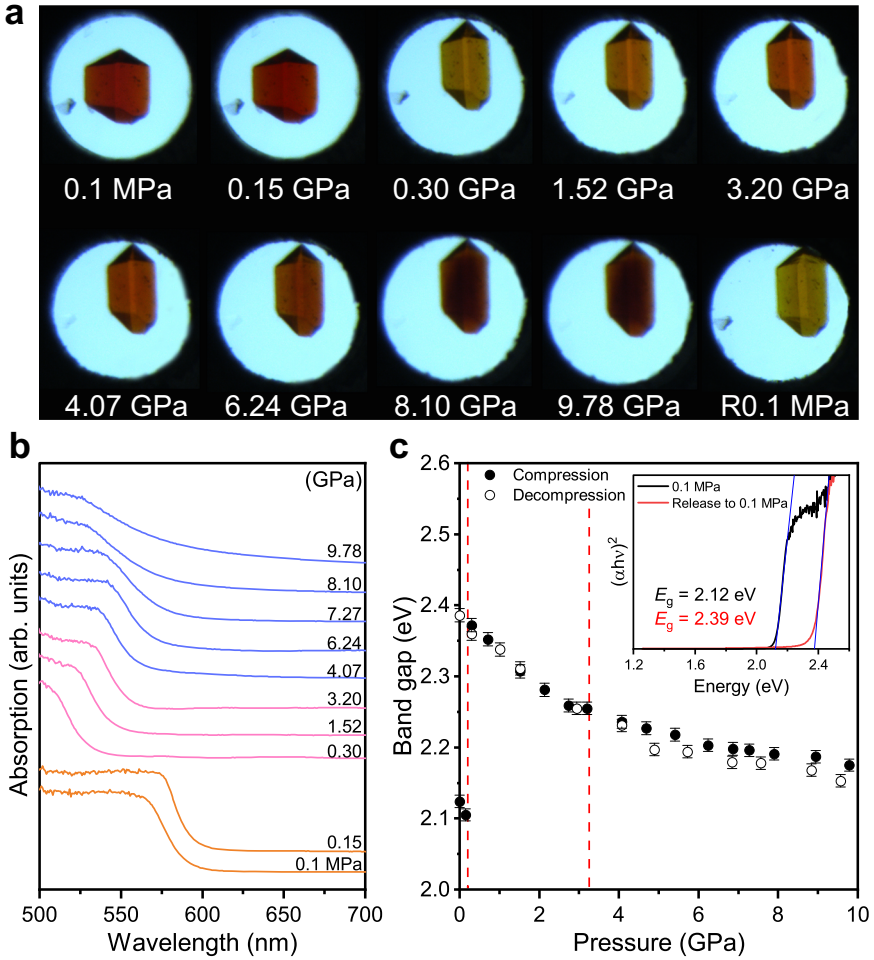

Fig. 4 | Optical properties of (MV)$BiBr_5$ at different pressures. a Optical images of a single crystal under pressure. The R0.1 MPa indicates the image when the pressure was completely released to the ambient pressure. **b** Evolution of the absorption spectra under compression. **c** Variations in the band gap of the sample under pressure. The inset shows the band gap of phase β (at 0.1 MPa) and phase γ released to ambient pressure at room temperature. Note that the error bars were obtained from the Tauc plot of the absorption spectra.

the band gap measured at 2.39 eV (Fig. 4a). Therefore, we used the pressure engineering strategy to synthesize a new phase of (MV)$BiBr_5$. As shown in Supplementary Fig. 14, the photoluminescence (PL) spectra exhibit a red shift of the PL peaks under compression, which is consistent with the observed changes in band gaps. The PL spectra of the sample exhibit red shift within the β phase region, a sudden blue shift appears during the β-γ phase transition. When the pressure is increased to 9.14 GPa, the PL spectra show an obvious redshift with a shift rate of 2.15 nm/GPa (Supplementary Fig. 14). It is noteworthy that the PL spectra could not be recovered after the pressure was released to ambient pressure, indicating an irreversible γ-β phase transformation. However, the crystal can return to its original spectra if mechanical stimulation is applied (Supplementary Fig. 14b). These observations are well consistent with the aforementioned XRD and absorption measurements.

The electronic structures of (MV)$BiBr_5$ at selected pressures were theoretically calculated by using both the PBE and HSE06 functionals. The results indicate that the β and γ phases are direct semiconductors, with both the valence band maximum (VBM) and conduction band minimum (CBM) located at the Y_2 point (Fig. 5). The ambient pressure band gaps obtained from the HSE06 (PBE) level for the β and γ phases are 1.89 (1.08) eV and 2.04 (1.18) eV, respectively. In contrast to the PBE method, the band gaps calculated at the HSE06 level give a better agreement with the experimental results of 2.12 eV (β phase) and 2.39 eV (γ phase), thereby validating the higher accuracy of the HSE06 functional. The band dispersions based on the HSE06 level are nearly identical to those obtained on the PBE level, with the exception that the conduction and valence bands are somewhat shifted away from the Fermi level due to the corrected gaps (see Supplementary Fig. 15). As shown in Fig. 5, the CBM in phase β at 0.1 MPa is primarily comprised of C-2p, Bi-6p, and N-2p states, whereas the main constituents in phase γ are C-2p and N-2p states. The VBM is mainly dominated by Br-4p state with a minor contribution from the Bi-6s state in phase β, whereas such small contribution disappears in phase γ due to the emergence of the Bi $6s^2$ lone pair expression. This unique feature differs from that of conventional hybrid halide perovskites, in which the VBM is mainly composed of B-cation *n*s and halide *n*p states and the CBM is predominantly contributed by the B-cation *n*p state, with negligible contributions from the organic moieties[59,60]. In the γ phase, the Bi1•••Br5′ bond lengths are gradually shortened and the CH•••Br hydrogen interactions are strongly enhanced under compression, which increases the orbital overlap between the Br-4p, C-2p and N-2p states, and thereby narrows the band gap (that is, 1.64 eV at 3.02 GPa for HSE06 calculations). Interestingly, we observe the gradual shift of the Bi-6p and Br-4p orbitals towards the Fermi level as the pressure is increased in phase γ (Fig. 5b–d), which is consistent with the large reduction in Bi1•••Br5′ bond distances (Fig. 2c).

To visualize the lone pair electrons on the Bi atoms, the electron localization function (ELF) calculations of β and γ phases are presented in Supplementary Fig. 16. In the case of phase β at

https://doi.org/10.1038/s41467-024-50961-2

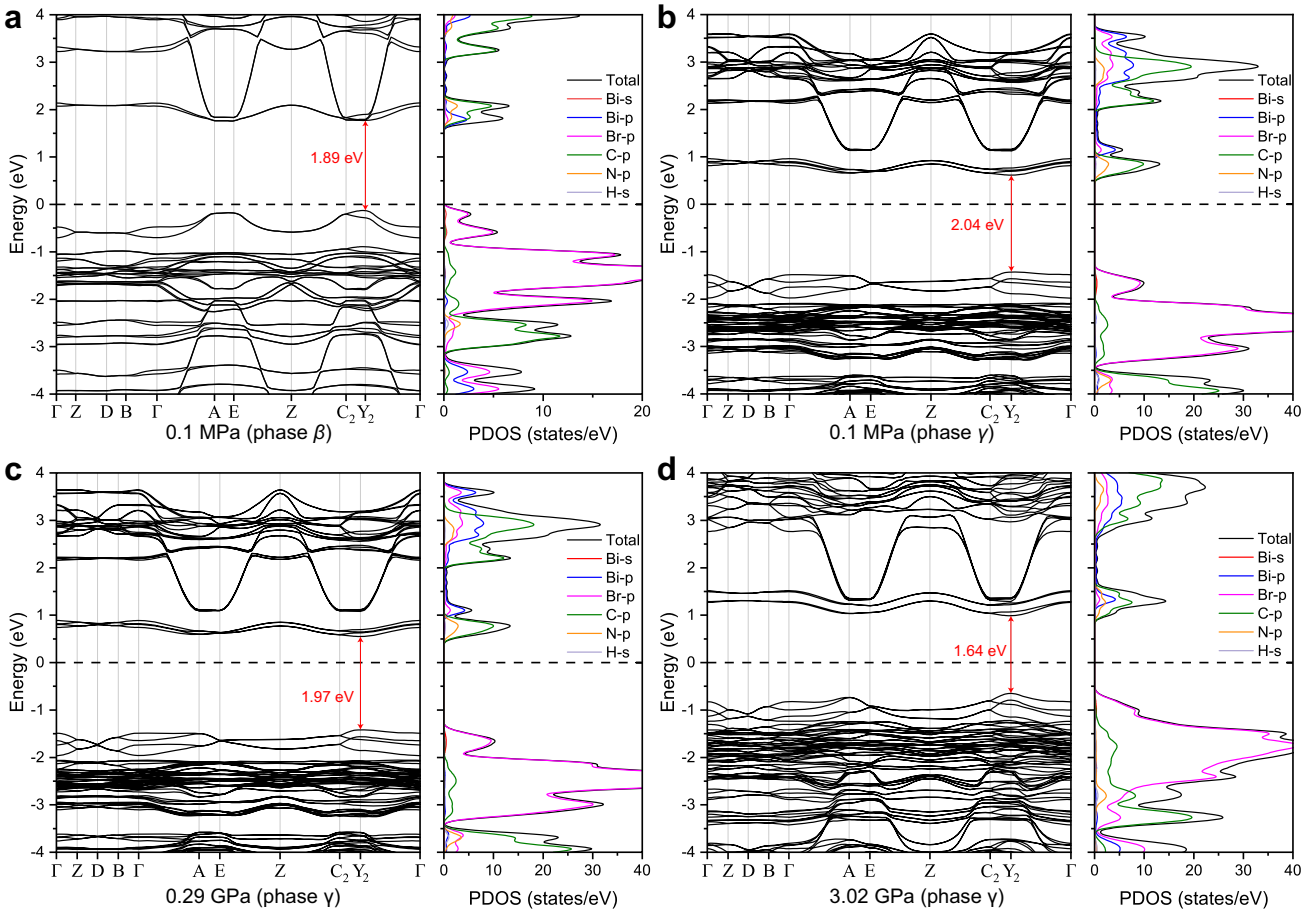

Fig. 5 | The electronic structures of (MV)$BiBr_5$ at selective pressures calculated by using HSE06 functional. a β phase at 0.1 MPa; **b**–**d** γ phase at 0.1 MPa, 0.29 GPa and 3.02 GPa. Note that the PDOS stands for projected density of states. The Fermi level is set to 0 eV.

0.1 MPa, we observe a strong covalency between Bi and Br atoms, indicating the absence of lone pair expression due to the short Bi-Br bond length. Inversely, a lobe-shaped ELF feature appears around Bi atom in phase γ, indicating that the orientations of the lone pair electrons should be toward the [100] direction (that is, along the 1D $BiBr_5$ chain). With increasing pressure, the lobe-like shape around the Bi atom becomes smaller, revealing the stereochemical activity of the Bi^{3+} lone pair electron is suppressed due to the shortened Bi1•••Br5′ distance (see Supplementary Fig. 16c). Moreover, in order to check whether the sudden increase of the Bi-Br bond distance in phase γ results in a change of Bi oxidation state under pressure, we performed a Bader charge analysis (Supplementary Table 6). The results show that the charges on the Bi1 atom in the phases β and γ are comparable at 0.1 MPa (3.629*e* vs 3.640*e*), and this magnitude remained almost the same as the pressure increases to 3.02 GPa (3.639e), revealing that the trivalent nature of the Bi1 atoms is maintained at high pressure. Additionally, the average charge on the Br atom becomes slightly less negative with increasing pressure in the phase γ region (−0.588e vs −0.568e).

In this work, we present the dynamic behavior of the 1D hybrid halide (MV)$BiBr_5$, which undergoes a pressure-induced irreversible SC-to-SC transition with a remarkable 20–30% elongation in length and a color change from red to dark yellow with an increase in band gap by 0.26 eV. Notably, the backward transition can be completely driven by mechanical stimulation rather than decompression. The combination of two types of SC-to-SC phase transitions enables the reversible structural and color alternations. Generally, hybrids of this kind are conventionally regarded as robust compounds, but the material studied here demonstrates excellent mechanical responsive feature. From the detailed single crystal structure analysis and electronic structures calculations, we find that the activation of the Bi^{3+} lone pair stereochemical activity leads to the elongation of the 1D $BiBr_5$ chains along the *a* axis and a slightly wider band gap. Meanwhile, half of the planar MV^{2+} cations undergo an almost 90° rotation relative to the *ab* plane together with the newly formed strong CH···Br hydrogen bonds are thus considered to play a significant role in the noticeable shape and color changes as observed. To the best of our knowledge, this is the extremely rare observation of a 1D hybrid halide that behaves similarly to dynamic organic crystals and metal complexes, providing new insights for the design of novel stimuli-responsive materials.

Methods

Synthesis of (MV)$BiBr_5$ single crystals

The (MV)$BiBr_5$ single crystals were synthesized using a traditional hydrothermal method as reported previously[34,35]. 0.5 mmol $BiBr_3$ (98%, Aladdin) and 0.5 mmol 4,4′-bipyridine (98%, Aladdin) were placed in the lining of a 25 mL hydrothermal reaction autoclave, then 2 mL 48% hydrobromic acid, and 3 mL methanol were added, stirred for ~15 min and the autoclave was then sealed. The autoclave was heated to 423 K over 2 h, maintained at this temperature for 72 h, and then slowly cooled to room temperature at a rate of 5 K/h. Finally, red block (MV)$BiBr_5$ single crystals were finally obtained by rapid washing with ethanol.

Single crystal and powder X-ray diffraction measurements

The ambient pressure single crystal X-ray diffraction data of (MV)$BiBr_5$ were collected on the Rigaku XtaLAB Synergy-R diffractometer equipped with graphite monochromatic Mo$K\alpha$ radiation (λ = 0.71073 Å). The

single crystal structure was solved by direct method using the SHELXS program[61], and refined by full-matrix least-squares optimization on F^2 using SHELXL program on OLEX2[62].

High-pressure single crystal X-ray diffraction (SXRD) data of (MV)$BiBr_5$ were collected on a Bruker D8 Venture diffractometer with Phonon II detector, fixed-chi goniometer and Incoatec IμS 3.0 AgKα microfocus source with Helios AgKα radiation (λ = 0.56086 Å). High-pressure X-ray data were collected by using eight different ω scans and an exposure time of 60 s for each frame. A single crystal with dimensions of 0.15 × 0.12 × 0.07 mm^3 was loaded into a diamond anvil cell (DAC) chamber, neon gas was used as pressure transmitting medium (PTM). The diameter of the diamond anvil culet is 500 μm and the aperture opening angle is 80°. The stainless-steel foil was pre-indented to a thickness of ~100 μm and the hole was laser drilled to a diameter about 230 μm. The DAC was mounted on the motorized XYZ stage attached to the Omega platform. The pressure was calibrated using the ruby fluorescence method with an accuracy of 0.03-0.05 GPa before and after each X-ray data acquisition[63]. A total of 12 high-pressure points were measured, ranging from 0.15 GPa to 5.26 GPa at room temperature. Data collection, indexing and reduction were performed using the APEX3 software. Structure refinements were performed using SHELXL-97 software. The selected crystallographic details at variable pressures are listed in Table S2. In addition, the EoSFit7c software was used to perform the least-squares fitting of V(P) data using the third-order Birch-Murnaghan equation of states (EoS) for phase γ of (MV)$BiBr_5$[64].

High-pressure angle-dispersive powder X-ray (PXRD) measurements were collected on the BL04-MSPD beamline at the ALBA Synchrotron using a monochromatic beam wavelength λ = 0.4246 Å. The X-ray data were recorded on an SX165 Rayonix Mar charge-coupled device (CCD) detector. Silicone oil was employed as the pressure transmitting medium and a small piece of Au was used for the pressure calibration. A membrane system coupled with a symmetric DAC was used to control the pressure. The collected diffraction images were integrated using the *Dioptas* 0.5.1 software[65], and XRD patterns were fitted by the Le Bail fitting method using GSAS-EXPGUI package[66]. The single crystal structures of (MV)$BiBr_5$ were used as the starting models to carry out all the data refinements.

Compressibility measurements

In order to gain a comprehensive understanding of the phase transitions of (MV)$BiBr_5$, ten single crystals were compressed at different compressibility rates at room temperature. A double membrane system coupled with a symmetric DAC with a large culet size (diameter: 600 μm) is used for the continuous compression/decompression. The pressure is determined by the online ruby system and the videos (Supplementary Movies 1–4) were recorded simultaneously. In certain cases (particularly for the decompression paths), if the DAC chamber pressure fails to reach the ambient pressure when the membrane gas pressure is completely released, the screws of the symmetric DAC are manually loosened.

High-pressure UV-vis absorption spectroscopy

High pressure in situ UV-vis absorption measurements of (MV)$BiBr_5$ single crystal were performed in a home-built spectroscopy system using a deuterium-halogen lamp 2-in-1 light source in the range of 300-1200 nm. Silicone oil (10 cSt) was used as PTM. The direct band gap values are determined by extrapolating the linear part of the $(\alpha h\nu)^2$ versus $h\nu$ curve, where α is the absorption coefficient, h is the Planck constant, and ν is the frequency of the photon.

High-pressure photoluminescence spectroscopy

High-pressure in situ photoluminescence (PL) measurements of (MV)$BiBr_5$ were conducted in a home-built spectroscopy system using an Ocean Optics QE series spectrometer. Silicone oil (10 cSt) was used as the PTM. A 532 nm green laser was used as the PL excitation source.

Second harmonic generation measurements

Second harmonic generation (SHG) measurements were employed to confirm the presence of an inversion center in the crystal structure of (MV)$BiBr_5$. The measurements were conducted using a home-designed goLite Solution-NLO optical system. A pulsed fiber laser (Rainbow1064Pro, 1064 nm, 20 MHz, <15 ps) was used as the excitation light source. A 50× objective was used to focus the laser with a laser spot of 10 μm in diameter. A spectrometer (NVOA2S-EX) was used to collect the SHG signal. Silicone oil was used as the PTM. The system was validated using a small KH_2PO_4 (KDP) single crystal. The results show the absence of SHG signals in both ambient and high-pressure phases of (MV)$BiBr_5$ (Supplementary Fig. 2), revealing that the centrosymmetric nature of the high pressure phase, consistent with the space group $P2_1/c$ as determined by single crystal X-ray diffraction measurements.

Theoretical calculations

Density functional theory (DFT) calculations including density of states, band structure, elastic constants, electron localization functions (ELFs) as well as Bader charges of (MV)$BiBr_5$ at selective pressures were performed using the projector augmented wave (PAW) method[67,68], as implemented in the Vienna Ab initio Simulation Package (VASP)[69,70]. The PBE exchange-correlation functional[71], with a 400 eV plane-wave cutoff for both phases β and γ was adopted. In the structure optimizations, the 6 × 2 × 3 and 5 × 2 × 2 k-points were utilized for phases β and γ, respectively, and the Hellmann-Feynman force acting on each atom is less than 0.01 eV/ Å. In electronic structures and energy calculations, a denser Monkhorst-Pack grid of 14 × 5 × 5 and 15 × 5 × 8 in the Brillouin zone was adopted for β and γ phases, respectively. Since the PBE functionals usually underestimate the band gap, the HSE06 hybrid functional was utilized to correct the band gap and dispersion. In order to clarify the irreversible phase transition mechanism from γ to β phase, the climbing-image nudged elastic band (CI-NEB) method was adopted to evaluate the kinetic barrier of the phase transition. Seven intermediate state configurations were generated by using the interpolation method in the CI-NEB calculations[72]. High-symmetry points of Γ, Z, D, B, A, E, C_2 and Y_2 in the Brillouin zones correspond to (0, 0, 0), (0, 0.5, 0), (0, 0.5, 0.5), (0, 0, 0.5), (−0.5, 0, 0.5), (−0.5, 0.5, 0.5), (−0.5, 0.5, 0), and (−0.5, 0, 0) points for phases β and γ for band structure calculations, respectively. The Bi $5d^{10}6s^26p^3$, Br $4s^24p^5$, C $2s^22p^2$, N $2s^22p^3$, and H $1s^1$ were explicitly treated as valence electrons. All calculations were performed using the experimental unit-cell lattice parameters obtained from the SXRD measurements, while the atomic positions within the lattice were optimized.

Data availability

The data supporting the findings of this study are available within the main text and the Supplementary Information file. Source data are provided with this paper. Crystallographic data for structures reported in this paper have been deposited in the Cambridge Crystallographic Data Center under reference numbers CCDC 2324652 – 2324662. These data can be obtained free of charge via www.ccdc.cam.ac.uk/data_request/cif. Supplementary information is available for this paper. Source data are provided with this paper.

References

1. Commins, P., Desta, I. T., Karothu, D. P., Panda, M. K. & Naumov, P. Crystals on the move: mechanical effects in dynamic solids. *Chem. Commun.* **52**, 13941–13954 (2016).
2. Naumov, P., Chizhik, S., Panda, M. K., Nath, N. K. & Boldyreva, E. Mechanically responsive molecular crystals. *Chem. Rev.* **115**, 12440–12490 (2015).

3. Naumov, P. et al. The rise of the dynamic crystals. *J. Am. Chem. Soc.* **142**, 13256–13272 (2020).
4. Sato, O. Dynamic molecular crystals with switchable physical properties. *Nat. Chem.* **8**, 644–656 (2016).
5. Chung, H. et al. Rotator side chains trigger cooperative transition for shape and function memory effect in organic semiconductors. *Nat. Commun.* **9**, 278 (2018).
6. Yao, Z.-S. et al. Molecular motor-driven abrupt anisotropic shape change in a single crystal of a Ni complex. *Nat. Chem.* **6**, 1079–1083 (2014).
7. Sahoo, S. C. et al. Kinematic and mechanical profile of the self-actuation of thermosalient crystal twins of 1,2,4,5-tetrabromobenzene: a molecular crystalline analogue of a bimetallic strip. *J. Am. Chem. Soc.* **135**, 13843–13850 (2013).
8. Karothu, D. P. et al. Exceptionally high work density of a ferroelectric dynamic organic crystal around room temperature. *Nat. Commun.* **13**, 2823 (2022).
9. Su, S.-Q. et al. Assembling an alkyl rotor to access abrupt and reversible crystalline deformation of a cobalt(II) complex. *Nat. Commun.* **6**, 8810 (2015).
10. Boldyreva, E., Kivikoski, J. & Howard, J. A. K. Distortion of crystal structures of some Co^{III} ammine complexes. II. distortion of crystal structures of $[Co(NH_3)_5NO_2]X_2$ (X = Cl, Br) on cooling. *Acta Crystallogr., Sect. B* **53**, 405–414 (1997).
11. Li, L. et al. Martensitic organic crystals as soft actuators. *Chem. Sci.* **10**, 7327–7332 (2019).
12. Liu, G., Liu, J., Liu, Y. & Tao, X. Oriented single-crystal-to-single-crystal phase transition with dramatic changes in the dimensions of crystals. *J. Am. Chem. Soc.* **136**, 590–593 (2014).
13. Sun, Y., Lei, Y., Dong, H., Zhen, Y. & Hu, W. Solvatomechanical bending of organic charge transfer cocrystal. *J. Am. Chem. Soc.* **140**, 6186–6189 (2018).
14. Iyoda, M. et al. Reversible color and shape changes of nanostructured fibers of a macrocyclic π-extended thiophene hexamer promoted by adsorption and desorption of organic vapor. *J. Am. Chem. Soc.* **142**, 13662–13666 (2020).
15. Jones, E. C. L., Bebiano, S. S., Ward, M. R., Bimbo, L. M. & Oswald, I. D. H. Pressure-induced superelastic behaviour of isonicotinamide. *Chem. Commun.* **57**, 11827–11830 (2021).
16. Kobatake, S., Takami, S., Muto, H., Ishikawa, T. & Irie, M. Rapid and reversible shape changes of molecular crystals on photoirradiation. *Nature* **446**, 778–781 (2007).
17. Ito, H. et al. Mechanical stimulation and solid seeding trigger single-crystal-to-single-crystal molecular domino transformations. *Nat. Commun.* **4**, 2009 (2013).
18. Liu, J. et al. The role of weak interactions in the mechano-induced single-crystal-to-single-crystal phase transition of 8-hydroxyquinoline-based co-crystals. *Chem. Asian J.* **11**, 1682–1687 (2016).
19. Gao, F.-F. et al. Pressure-tuned multicolor emission of 2D lead halide perovskites with ultrahigh color purity. *Angew. Chem. Int. Ed.* **62**, e202218675 (2023).
20. Zhang, L., Wang, K., Lin, Y. & Zou, B. Pressure effects on the electronic and optical properties in low-dimensional metal halide perovskites. *J. Phys. Chem. Lett.* **11**, 4693–4701 (2020).
21. Gao, F.-F. et al. Dual-stimuli-responsive photoluminescence of enantiomeric two-dimensional lead halide perovskites. *Adv. Opt. Mater.* **9**, 2100003 (2021).
22. Mao, Y. et al. Pressure-modulated anomalous organic–inorganic interactions enhance structural distortion and second-harmonic generation in $MHyPbBr_3$ perovskite. *J. Am. Chem. Soc.* **145**, 23842–23848 (2023).
23. Liu, S. et al. Manipulating efficient light emission in two-dimensional perovskite crystals by pressure-induced anisotropic deformation. *Sci. Adv.* **5**, eaav9445 (2019).
24. Sun, M.-E. et al. Chirality-dependent structural transformation in chiral 2D perovskites under high pressure. *J. Am. Chem. Soc.* **145**, 8908–8916 (2023).
25. Stoumpos, C. C., Mao, L., Malliakas, C. D. & Kanatzidis, M. G. Structure–band gap relationships in hexagonal polytypes and low-dimensional structures of hybrid tin iodide perovskites. *Inorg. Chem.* **56**, 56–73 (2017).
26. Fabini, D. H. et al. Dynamic stereochemical activity of the Sn^{2+} lone pair in perovskite $CsSnBr_3$. *J. Am. Chem. Soc.* **138**, 11820–11832 (2016).
27. Wang, S., Mitzi, D. B., Feild, C. A. & Guloy, A. Synthesis and characterization of $[NH_2C(I)=NH_2]_3MI_5$ (M = Sn, Pb): stereochemical activity in divalent tin and lead halides containing single <110>perovskite sheets. *J. Am. Chem. Soc.* **117**, 5297–5302 (1995).
28. Zhang, L. et al. Manipulating lone-pair-driven luminescence in 0D tin halides by pressure-tuned stereochemical activity from static to dynamic. *Angew. Chem. Int. Ed.* **62**, e202311912 (2023).
29. Huang, X. et al. Understanding electron–phonon interactions in 3D lead halide perovskites from the stereochemical expression of $6s^2$ lone pairs. *J. Am. Chem. Soc.* **144**, 12247–12260 (2022).
30. Li, X., Guan, Y., Li, X. & Fu, Y. Stereochemically active lone pairs and nonlinear optical properties of two-dimensional multilayered tin and germanium iodide perovskites. *J. Am. Chem. Soc.* **144**, 18030–18042 (2022).
31. Yangui, A. et al. Rapid and robust spatiotemporal dynamics of the first-order phase transition in crystals of the organic-inorganic perovskite $(C_{12}H_{25}NH_3)_2PbI_4$. *Sci. Rep.* **5**, 16634 (2015).
32. Zhang, R. et al. Effects of nonhydrostatic stress on structural and optoelectronic properties of methylammonium lead bromide perovskite. *J. Phys. Chem. Lett.* **8**, 3457–3465 (2017).
33. Szafrański, M. & Katrusiak, A. Photovoltaic hybrid perovskites under pressure. *J. Phys. Chem. Lett.* **8**, 2496–2506 (2017).
34. Bi, W., Leblanc, N., Mercier, N., Auban-Senzier, P. & Pasquier, C. Thermally induced Bi(III) lone pair stereoactivity: ferroelectric phase transition and semiconducting properties of $(MV)BiBr_5$ (MV = methylviologen). *Chem. Mater.* **21**, 4099–4101 (2009).
35. Leblanc, N. et al. The motley family of polar compounds (MV)$[M(X_{5-x}X'_x)]$ based on anionic chains of trans-connected $M(III)(X,X')_6$ octahedra (M = Bi, Sb; X, X'=Cl, Br, I) and methylviologen (MV) dications. *J. Solid State Chem.* **195**, 140–148 (2012).
36. Fisch, M., Lanza, A., Boldyreva, E., Macchi, P. & Casati, N. Kinetic control of high-pressure solid-state phase transitions: a case study on L-serine. *J. Phys. Chem. C* **119**, 18611–18617 (2015).
37. Zakharov, B. A., Tumanov, N. A. & Boldyreva, E. V. β-Alanine under pressure: towards understanding the nature of phase transitions. *CrystEngComm* **17**, 2074–2079 (2015).
38. Park, S. K. & Diao, Y. Martensitic transition in molecular crystals for dynamic functional materials. *Chem. Soc. Rev.* **49**, 8287–8314 (2020).
39. Herbstein, F. On the mechanism of some first-order enantiotropic solid-state phase transitions: from Simon through Ubbelohde to Mnyukh. *Acta Crystallogr. Sect. B* **62**, 341–383 (2006).
40. Fu, B. et al. Pressure-induced ferroelastic transition drives a large shape change in a Ni(II) complex single crystal. *J. Phys. Chem. Lett.* **14**, 3891–3897 (2023).
41. Cai, W. et al. Giant negative area compressibility tunable in a soft porous framework material. *J. Am. Chem. Soc.* **137**, 9296–9301 (2015).
42. Shi, Y. et al. Pressure-induced emission (PIE) of one-dimensional organic tin bromide perovskites. *J. Am. Chem. Soc.* **141**, 6504–6508 (2019).
43. Fang, Y. et al. Harvesting high-quality white-light emitting and remarkable emission enhancement in one-dimensional halide perovskites upon compression. *JACS Au* **1**, 459–466 (2021).

44. Gaillac, R., Pullumbi, P. & Coudert, F.-X. ELATE: an open-source online application for analysis and visualization of elastic tensors. *J. Condens. Matter Phys.* **28**, 275201 (2016).
45. Wei, W. et al. An unusual phase transition driven by vibrational entropy changes in a hybrid organic–inorganic perovskite. *Angew. Chem. Int. Ed.* **57**, 8932–8936 (2018).
46. Li, K. et al. Origin of ferroelectricity in two prototypical hybrid organic–inorganic perovskites. *J. Am. Chem. Soc.* **144**, 816–823 (2022).
47. Gu, J. et al. Correlating photophysical properties with stereochemical expression of $6s^2$ lone pairs in two-dimensional lead halide perovskites. *Angew. Chem. Int. Ed.* **62**, e202304515 (2023).
48. Cruz-Cabeza, A. J., Reutzel-Edens, S. M. & Bernstein, J. Facts and fictions about polymorphism. *Chem. Soc. Rev.* **44**, 8619–8635 (2015).
49. Kapil, V. & Engel, E. A. A complete description of thermodynamic stabilities of molecular crystals. *Proc. Natl Acad. Sci. USA* **119**, e2111769119 (2022).
50. Seki, T., Sakurada, K. & Ito, H. Controlling mechano- and seeding-triggered single-crystal-to-single-crystal phase transition: molecular domino with a disconnection of aurophilic bonds. *Angew. Chem. Int. Ed.* **52**, 12828–12832 (2013).
51. Jin, M., Sumitani, T., Sato, H., Seki, T. & Ito, H. Mechanical-stimulation-triggered and solvent-vapor-induced reverse single-crystal-to-single-crystal phase transitions with alterations of the luminescence color. *J. Am. Chem. Soc.* **140**, 2875–2879 (2018).
52. Robinson, K., Gibbs, G. V. & Ribbe, P. H. Quadratic elongation: a quantitative measure of distortion in doordination polyhedra. *Science* **172**, 567–570 (1971).
53. Brown, I. D. Bond valence as an aid to understanding the stereochemistry of O and F complexes of Sn(II), Sb(III), Te(IV), I(V) and Xe(VI). *J. Solid State Chem.* **11**, 214–233 (1974).
54. Shang, R., Chen, S., Wang, B.-W., Wang, Z.-M. & Gao, S. Temperature-induced irreversible phase transition from perovskite to diamond but pressure-driven back-transition in an ammonium copper formate. *Angew. Chem. Int. Ed.* **55**, 2097–2100 (2016).
55. Knutson, J. L., Martin, J. D. & Mitzi, D. B. Tuning the band gap in hybrid tin iodide perovskite semiconductors using structural templating. *Inorg. Chem.* **44**, 4699–4705 (2005).
56. Takahashi, Y., Obara, R., Nakagawa, K., Nakano, M., Tokita, J.-Y. & Inabe, T. Tunable charge transport in soluble organic–inorganic hybrid semiconductors. *Chem. Mater.* **19**, 6312–6316 (2007).
57. Fu, Y. Stabilization of metastable halide perovskite lattices in the 2D limit. *Adv. Mater.* **34**, 2108556 (2022).
58. Katan, C., Mercier, N. & Even, J. Quantum and dielectric confinement effects in lower-dimensional hybrid perovskite semiconductors. *Chem. Rev.* **119**, 3140–3192 (2019).
59. Smith, M. D. & Karunadasa, H. I. White-light emission from layered halide perovskites. *Acc. Chem. Res.* **51**, 619–627 (2018).
60. Jakubas, R. et al. Ferroelectricity in ethylammonium bismuth-based organic–inorganic hybrid: $(C_2H_5NH_3)_2[BiBr_5]$. *Inorg. Chem.* **59**, 3417–3427 (2020).
61. Sheldrick, G. M. A. Short history of SHELX. *Acta Crystallogr. Sect. A* **64**, 112 (2008).
62. Dolomanov, O. V., Bourhis, L. J., Gildea, R. J., Howard, J. A. K. & Puschmann, H. OLEX2: a complete structure solution, refinement and analysis program. *J. Appl. Crystallogr.* **42**, 339–341 (2009).
63. Mao, H. K., Xu, J. & Bell, P. M. Calibration of the ruby pressure gauge to 800 kbar under quasi-hydrostatic conditions. *J. Geophys. Res.* **91**, 4673–4676 (1986).
64. Angel, R. J., Alvaro, M. & Gonzalez-Platas, J. EosFit7c and a Fortran module (library) for equation of state calculations. *Z. Kristallogr.* **229**, 405–419 (2014).
65. Prescher, C. & Prakapenka, V. B. DIOPTAS: a program for reduction of two-dimensional X-ray diffraction data and data exploration. *High. Press. Res.* **35**, 223–230 (2015).
66. Toby, B. EXPGUI, a graphical user interface for GSAS. *J. Appl. Crystallogr.* **34**, 210–213 (2001).
67. Blöchl, P. E. Projector augmented-wave method. *Phys. Rev. B.* **50**, 17953–17979 (1994).
68. Kresse, G. & Joubert, D. From ultrasoft pseudopotentials to the projector augmented-wave method. *Phys. Rev. B.* **59**, 1758–1775 (1999).
69. Kresse, G. & Furthmüller, J. Efficient iterative schemes for ab initio total-energy calculations using a plane-wave basis set. *Phys. Rev. B.* **54**, 11169–11186 (1996).
70. Kresse, G. & Furthmüller, J. Efficiency of ab-initio total energy calculations for metals and semiconductors using a plane-wave basis set. *Comput. Mater. Sci.* **6**, 15–50 (1996).
71. Perdew, J. P. et al. Restoring the Density-Gradient Expansion for Exchange in Solids and Surfaces. *Phys. Rev. Lett.* **100**, 136406 (2008).
72. Henkelman, G., Uberuaga, B. P. & Jónsson, H. A climbing image nudged elastic band method for finding saddle points and minimum energy paths. *J. Chem. Phys.* **113**, 9901–9904 (2000).

Acknowledgements

This work is financially supported by the National Natural Science Foundation of China (No. 12274062) and the Natural Science Foundation of Sichuan Province (No. 2022NSFSC0297). The authors would like to thank Dr. Dongzhou Zhang (GeoSoilEnviroCARS, University of Chicago) and Prof. Wei Li (Nankai University) for their fruitful discussions. The authors would also like to acknowledge Qiaoqiao Li for her help with the HSE06 calculations. Weiyi Wang and Prof. Ling Huang at Sichuan Normal University for assistance with the ambient pressure single crystal X-ray diffraction measurements. High-pressure powder XRD experiments were performed at BL04-MSPD beamline at ALBA Synchrotron with the collaboration of ALBA staff and we thank Dr. Catalin Popescu for the experimental support.

Author contributions

W.C. conceived and supervised the study. D.Z. synthesized single crystal samples and conducted high-pressure absorption measurements, and analyzed the single crystal X-ray data; B.F., F.L., L.W., and H.Liu. collected and analyzed the high-pressure single-crystal X-ray diffraction data. W.H. recorded the videos and processed the data. H.Li. and L.Z. performed the theoretical calculations. D.Z. and W.H. prepared the figures for the manuscript. This paper was written with the contributions from D.Z., W.H., and W.C., and all other authors contributed to editing the manuscript thereafter.

Competing interests

The authors declare no competing interests.

Additional information

Supplementary information The online version contains supplementary material available at https://doi.org/10.1038/s41467-024-50961-2.

Correspondence and requests for materials should be addressed to Liujiang Zhou or Weizhao Cai.

Peer review information *Nature Communications* thanks Kamil Dziubek, Panče Naumov and the other, anonymous, reviewer(s) for their contribution to the peer review of this work. A peer review file is available.